High Impact Toughness Polypropylene/$CaCO_3$ Nanocomposites and the Toughening Mechanism

Yong Lin,[†] Haibin Chen,[‡] Chi-Ming Chan,[†,*] and Jingshen Wu[‡]

Department of Chemical Engineering and Department of Mechanical Engineering, The Hong Kong University of Science and Technology, Clear Water Bay, Hong Kong

Received May 16, 2008; Revised Manuscript Received October 6, 2008

ABSTRACT: Considerable improvement in the impact toughness of an annealed polypropylene (PP) nanocomposite containing $CaCO_3$ nanoparticles was achieved and its toughening mechanism was investigated. The nanocomposite was prepared by melt-blending PP and $CaCO_3$ nanoparticles in a batch mixer. Injection-modeled impact and tensile bars were annealed at 150 °C for 2 h prior to the impact and tensile tests. The Young modulus and yield stress of the nanocomposite were found to increase after annealing. What is more, the annealed nanocomposite had much higher impact toughness than its unannealed counterpart. The average Izod impact strength of the 150 °C-annealed nanocomposite, containing 20 wt % (7.8 vol %) $CaCO_3$ nanoparticles coated with 6 wt % stearic acid, was 168 J/m, which was 3.5 times higher than that of neat PP. Experiments, including X-ray diffraction, differential scanning calorimetry, scanning electron microscopy (SEM) and the instrumented falling-weight impact test, were performed to study the toughening mechanism of the annealed nanocomposite. SEM micrographs of the impact fracture surface and bulk morphology underneath the fracture surface of the broken Izod samples and the results of the instrumented falling-weight impact test suggested that the plastic deformation zone that formed in the crack-initiation stage was responsible for the high impact toughness of the annealed nanocomposite. The micromorphology ahead of the arrested crack tip of the annealed nanocomposite showed that the propagation of the crack occurred through shear-to-rupture of the ligaments at the crack opening. The size of the plastic deformation zone and the fracture energy were likely related to the increased matrix ligament strength after annealing. In summary, the annealing-reinforced ligaments were proposed to be responsible for the high impact toughness of the annealed nanocomposite.

1. Introduction

Polypropylene (PP), one of the most widely used commodity plastics, has been the subject of intensive studies with the objective to improve its mechanical properties. PP composites with high modulus and impact strength, especially at low temperatures, are highly desirable for many industrial applications. Calcium carbonate, one of most commonly used inorganic fillers, has been used to improve the stiffness and impact toughness of PP. Many researchers have performed studies on the toughening mechanisms of calcium carbonate-filled PP.[1−8] It is generally agreed that cavitations, which are induced by debonding at the particle-matrix interface, release the triaxial tension state of the ligaments, resulting in massive plastic deformation, which is a substantial energy-absorbing process.[3,5,6,9] Many factors have been shown to control the ultimate impact strength of the composites, such as the size of inclusion,[3,4,10] the adhesion between the filler and the matrix,[2,11−13] and the crystalline morphology of the matrix.[14−17] However, the effects of the size of the calcium carbonate particles on the impact toughness of PP have not yet been clearly identified. Thio et al.[4] revealed that PP filled with 0.7-μm particles had high toughness while PP filled with 70-nm particles had reduced toughness. Their observations were replicated by Zuiderduin et al., who also found that 70-nm particles failed to toughen PP.[3] Thio et al. and Zuiderduin et al. attributed the failure of the 70-nm particles to toughen PP to their poor dispersion. In contrast with their results, Chan et al.[5] successfully used surface-modified 44-nm calcium carbonate particles to increase the Izod impact strength of PP up to 2.5 times. Observations using transmission electron microscopy (TEM) showed that nanoparticle agglomerates were broken down to primary particles during mixing, resulting in good dispersion of the nanoparticles. Another successful example of using calcium carbonate nanoparticles was presented by Wang et al.[18] They claimed that when the surfaces of calcium carbonate nanoparticles were uniformly coated with a surfactant, good dispersion was achieved, leading to high impact toughness of the nanocomposites. The discrepancies in the findings on the toughening effectiveness of calcium carbonate nanoparticles may be caused by their different degrees of dispersion in polymers. In order to achieve good dispersion, surface modification of the calcium carbonate nanoparticles is necessary. The surfactant selected should have weak interactions with the polymer matrix to facilitate interface debonding, which is important in releasing plastic constraints and improving the toughness of the nanocomposites.[2,13,19,20] To achieve good results, an optimum amount of surfactant should be used. Osman et al.[21] indicated that an excessive amount of coating led to a negative effect on the mechanical properties of the composites. In addition to the influence of nanoparticles, the mechanical properties of composites also depend on the morphology of the polymer.[14−17,22−26] One of the most obvious examples is that β PP has a higher impact toughness than α PP. Labour et al.[15] investigated the effect of the β crystalline phase on the mechanical properties of $CaCO_3$-filled PP and correlated the intrinsic molecular arrangement of the β phase with its low plastic deformation resistance. In addition, the crystalline morphology, including the lamellar thickness, crystallinity, spherulitic size and the perfection of the crystal domains, also influences the mechanical properties of PP.[23−26] Morphological changes in nanocomposites can be introduced simply by annealing them at elevated temperatures. The effects of annealing time and temperature on the microstructures of PP have been extensively studied,[23,25,27−29] although the results are mostly from neat PP. Due to the nucleation effect of nanosized

* Corresponding author. E-mail: kecmchan@ust.hk. Tel: 852-2358-7125. Fax: 852-2358-7125.
[†] Department of Chemical Engineering, The Hong Kong University of Science and Technology.
[‡] Department of Mechanical Engineering, The Hong Kong University of Science and Technology.

10.1021/ma801095d CCC: $40.75
Published on Web 11/11/2008

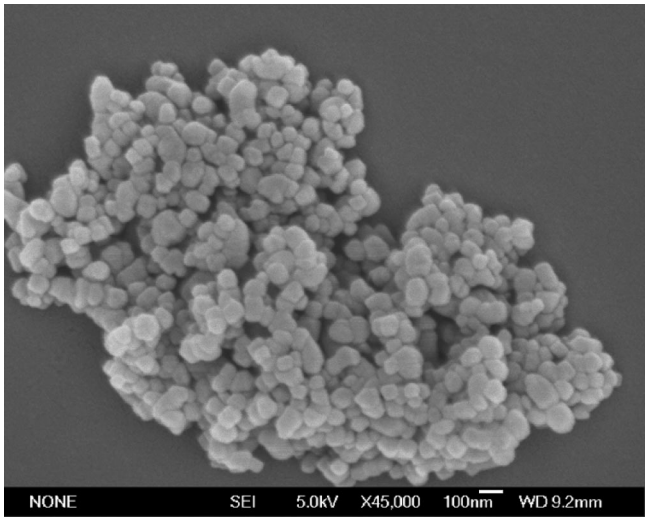

Figure 1. SEM micrograph of SPT.

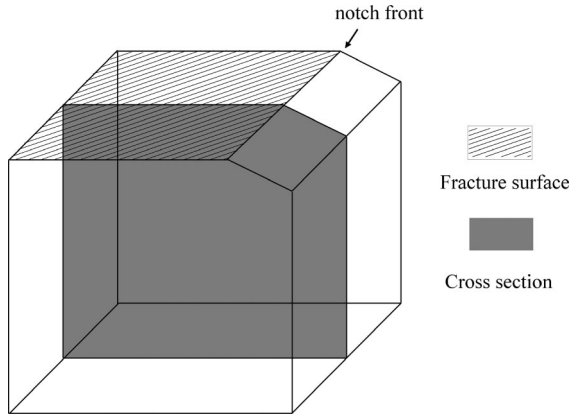

Figure 2. Schematic picture to show the fracture surface and the cross-section of a broken Izod sample for SEM observations.

particles, small and imperfect spherulites form as a result. The effects of annealing on refined spherulites may influence the mechanical properties of PP nanocomposites in different ways.

In this study, we used 70-nm calcium carbonate particles to toughen isotactic PP (i-PP). To ensure good dispersion, the nanoparticles were coated with a monolayer of stearic acid. The effects of annealing on the impact toughness of the calcium carbonate nanocomposites were found to be tremendous. The fracture mechanism of the annealed nanocomposites was investigated.

2. Experimental Section

2.1. Materials. Homopolymer i-PP was supplied by Samsung Company. Its melt flow index measured with an ASTM-D1238 was 5.0 g/10 min. Calcium carbonate nanoparticles, with a trade name of SPT, were provided by Solvay Chemical Company. The average particle size of SPT was determined to be about 70 ± 10 nm by measuring the sizes of the particles on a scanning electron microscopy (SEM) micrograph, as shown in Figure 1. An antioxidant (0.5 wt %), Irganox 1010, was added to the PP during compounding. The stearic acid was purchased from Sigma with a purity grade of 95%.

2.2. Surface Treatment of the Nanoparticles. SPT, as received, was coated with 2 wt % stearic acid. To improve its dispersion in the polymer matrix, the as-received SPT was further coated with stearic acid to increase its compatibility with the PP matrix and to minimize the interactions among the particles. The coating method was as follows. First, 10 g of SPT was mixed with a 40 mL solution mixture of water and ethanol in a volume ratio of 3:1. The

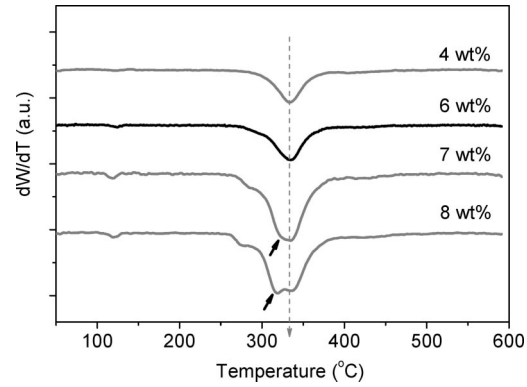

Figure 3. DTG curves of calcium carbonate nanoparticles coated with different amounts of stearic acid.

suspension was stirred by a magnetic stirrer for 2 h to completely wet the particles. Then, the suspension was heated to and maintained at 80 °C. A fixed amount of stearic acid dissolved in the ethanol solvent was gradually added to the suspension drop by drop. After 2 h of reaction time, surface-treated calcium carbonate particles, which settled at the bottom of the beaker, were dried in an oven at 105 °C overnight. The actual amount of stearic acid coated on the calcium carbonate particles was measured by a thermogravimetric analyzer (TGA). The measurement was conducted at a heating rate of 20 °C/min under compressed air flow.

2.3. Preparation and Characterization of the Nanocomposite. A nanocomposite containing 20 wt % (7.8 vol %) nanoparticles was prepared. PP and surface-treated $CaCO_3$ nanoparticles were blended in a Hakke mixer. The mixing time and temperature were 15 min and 180 °C, respectively. The rotor speed was 60 rpm and the detailed blending procedures were described previously.[5] The crystallization characteristics of the annealed and unannealed nanocomposites were studied by a Perkin-Elmer (Diamond 7) differential scanning calorimeter (DSC). The melting temperature and crystallinity were determined using a heating scan obtained at a heating rate of 10 °C/min. The crystallization temperature was determined from a cooling scan obtained at a cooling rate of 10 °C/min. The heat of fusion of the PP crystals was taken to be 209 J/g.[30] X-ray diffraction (XRD) spectra were obtained using a PANalytical X'Pert PRO operated at a voltage of 40 kV and with a current of 40 mA, using Cu Kα radiation ($\lambda = 1.54056$). A dwell time of 2 s per step was used. The dispersion state of the nanoparticles was examined by optical microscopy (OM). OM micrographs were taken from 10-μm thick thin films of the nanocomposites. The micromorphology of the nanocomposites was examined by TEM. Thin sections (~80 nm) of nanocomposites were cut using a Leica Ultract R microtome equipped with a diamond knife at room temperature. To reveal the lamellar structures, the nanocomposites were stained with RuO_4. The detailed procedures of ultramicrotomy and staining can found in the paper by Li et al.[31] The nanocomposites were melted at 200 °C for 10 min in a hot press and then pressure was applied for another 5 min to produce sheets with a thickness of 2.5 mm. After cooling down the sheets at the cooling rate of 20 °C/ min to room temperature, they were cut into 70 mm × 70 mm squares for testing.

2.4. Mechanical Test. The injection molding conditions of the impact and tensile bars were as described previously.[5] ASTM-D658 and ASTM-D256 methods were used to prepare the tensile and impact bars, respectively. The injection-molded tensile and impact bars were annealed in an oven at designated temperatures and for designated periods of time. After annealing, the samples were cooled in the ambient air. The annealed impact bars were stored at 23 ± 3 °C at a relative humidity of 50% for 24 h before notching. V-shaped notches were produced by a CSI automatic notcher (CS-93M). The cutter speed and the table feed rate were about 92 and 100 mm/min, respectively. The Izod impact tests were conducted one day after the samples were notched. Tensile-elongation measurements were performed one day after the tensile bars were

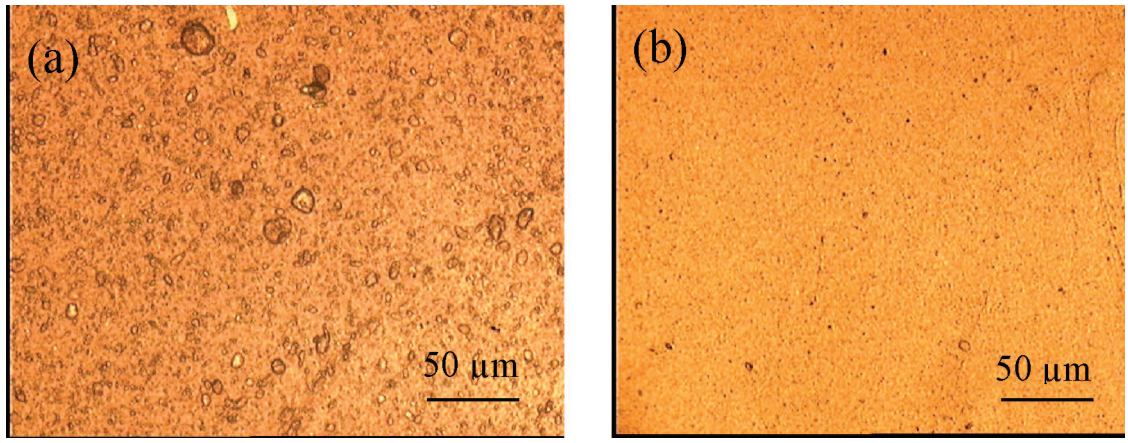

Figure 4. Optical micrographs showing the dispersion of nanoparticles (20 wt %) in the PP matrix: (a) the nanocomposite contains the as-received nanoparticles and (b) the nanocomposite contains the monolayer-coated nanoparticles.

annealed. A crosshead speed of 5 mm/min was used in the tensile tests. Instrumented falling-weight impact tests were conducted on a FRACTOVIS PLUS manufactured by CEAST. The impact weight was 3.0 Kg. A striker having a hemispheric head with a diameter of 20 mm was used. The impact velocity was 3 m/s.

2.5. Fractographs. The dimensions of the plastic deformation zone of the broken Izod samples were measured using SEM micrographs obtained on the fracture surface and the cross-section, as shown in Figure 2. The cross-section of the fractured Izod sample was produced by cryo-fracture. After immersing the sample in liquid nitrogen for more than 20 min, it was cleaved by a wedge immediately (less than 3 s) after it had been taken out of liquid nitrogen. To examine the crack-initiation stage, an arrested crack in an annealed sample was produced with a Charpy impact tester. The notched impact bars were placed on two supporters of the Charpy instrument as usual. The pendulum was raised at an angle of 90° from the vertical and then released to hit the sample. With an appropriately chosen weight, the sample was not broken into two halves and the propagating crack stopped in the interior of the sample. The method used to expose the morphology of the arrested crack in the bulk for the SEM observations was the same as the one used to expose the cross-section of the broken Izod sample. A block of the annealed nanocomposite containing the arrested crack was embedded by an epoxy matrix then was cut into thin sections (~ 80 nm) at room temperature using a Leica Ultract R microtome equipped with a diamond knife. The thin sections containing the arrested crack tip were examined with a JEOL 100CX II TEM operated at an accelerating voltage of 100 kV. SEM observations were performed on JEOL JSM-6390 or -6700F SEM. To prevent charging, the SEM samples were sputter-coated with gold.

3. Results and Discussion

3.1. Determination of Stearic Acid Coverage on SPT. The amount of coating on the particles has a great effect on their dispersion in a polymer matrix. Recently, Osman et al.[32] used differential thermal gravimetric analysis (DTG) to differentiate physisorbed from chemisorbed coatings on calcium carbonate particles. They found that if there is only one layer of chemisorbed coating, then only one decomposition peak appears in the DTG curve. If the coating is thicker than a monolayer, physisorbed layers will appear. As a result, a shoulder or even a new peak, depending on the amount of coating used, will emerge at a lower temperature. The critical amount of coating that is associated with the emergence of a shoulder can be regarded as the complete monolayer coating. The DTG traces of SPT particles with different coating amounts are displayed in Figure 3. For the 4 and 6 wt % coatings, a single peak appears at about 330 °C. The peak shifts to a lower temperature when the coating amount increases to 7 wt %. Therefore, a 6 wt % coating can be regarded as the correct amount needed for a complete monolayer coating. The amount of stearic acid needed for a monolayer coating can be also estimated theoretically using the fact that the surface area of SPT was reported by the supplier to be 22.2 m^2/g and each Ca^{2+} ion occupies an area of 0.2 nm^2, according to its crystal structure.[33] If each stearic acid molecule connects one Ca^{2+} ion and orients vertically to the particle surface,[34] the calculated amount of stearic acid that is needed to produce the complete monolayer coating is about 5.3 wt %. The calculated and DTG results show good agreement. In order to achieve good dispersion and to avoid the negative effect induced by excessive amounts of coating, nanosized calcium carbonate particles coated with 6 wt % stearic acid were used to prepare the PP nanocomposite.

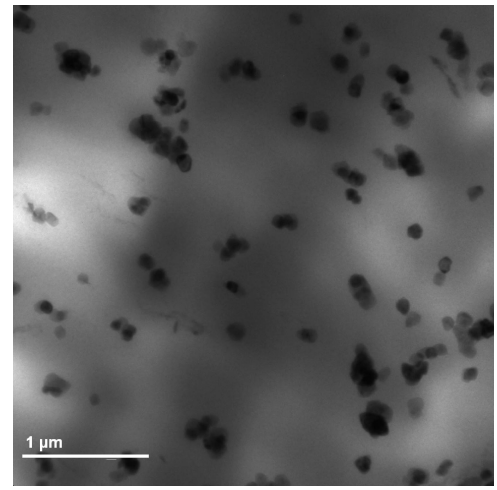

Figure 5. TEM micrograph showing the dispersion of the monolayer-coated nanoparticles in the PP matrix.

Table 1. Mechanical and Thermal Properties of i-PP and Nanocomposites with and without Heat Treatment

	Young's modulus (GPa)	yield stress (MPa)	Izod impact strength (J/m)	T_m (°C)	T_c (°C)	crystallinity (wt %)
PP	1.9 ± 0.1	36.3 ± 0.2	38 ± 3	166	115	34.6
annealed PP	2.1 ± 0.1	35.5 ± 0.3	45 ± 5	167	–	40.1
unannealed nanocomposite	2.7 ± 0.1	31.6 ± 0.4	51 ± 5	165	121	33.3
annealed nanocomposite	3.4 ± 0.1	33.5 ± 0.3	168 ± 10	164	–	41.4

3.2. Characterization of PP and Nanocomposites. The dispersion state of the nanoparticles in the PP matrix was examined by OM. The OM micrographs of the nanocomposites containing 20 wt % as-received nanoparticles and monolayer-

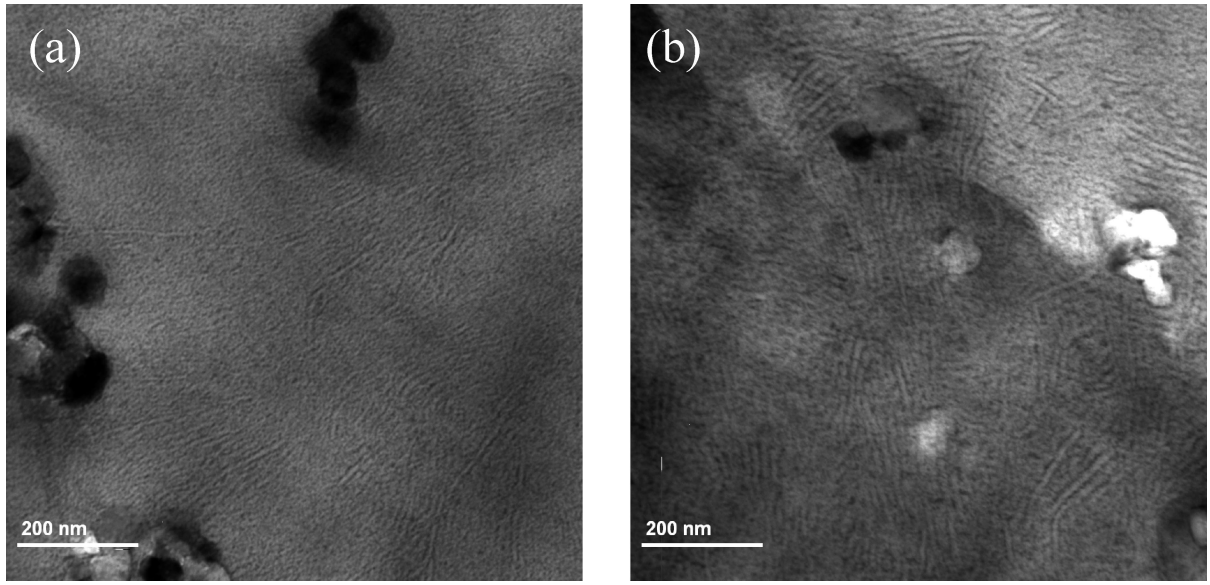

Figure 6. TEM micrographs showing the lamellar structures of the nanocomposites: (a) an unannealed nanocomposite and (b) an annealed nanocomposite.

coated nanoparticles are shown in Figure 4, parts a and b, respectively. The as-received nanoparticles formed large agglomerations in the PP matrix, as seen in Figure 4a. In contrast, when the nanoparticles were coated with a monolayer of stearic acid, no obvious agglomerations were observed, as evidenced in Figure 4b. This comparison clearly indicates that good dispersion can be achieved using the nanoparticles with a monolayer coating of stearic acid. The TEM micrograph, as shown in Figure 5, also reveals that the monolayer-coated nanoparticles were dispersed reasonably well in the PP matrix.

The mechanical and thermal properties of PP and nanocomposites with and without heat treatment are listed in Table 1. A noticeable change in the mechanical property after annealing is that the impact strength of the annealed nanocomposite increased by more than three times compared with that of the unannealed nanocomposite. The yield stresses of unannealed and annealed nanocomposites, which were lower than that of neat PP because of the debonding of the nanoparticles from the PP matrix,[35] indicates that the bonding strength between the PP and the nanoparticles is relatively weak. Due to the presence of $CaCO_3$ nanoparticles and debonding not occurring in the elastic region during the tensile test,[35] the Young's moduli of both the annealed and unannealed nanocomposites were higher than that of neat PP. No significant increase in the crystallinity of PP was observed after the addition of $CaCO_3$ nanoparticles while the crystallinity of the neat PP and nanocomposite increased by about 16 and 25 wt %, respectively, upon annealing, probably due to the thickening of lamellae, perfection of crystals and transformation of the β phase to the α phase, as discussed later. The increased crystallinity led to an increase in the Young's modulus and the yield stress of the annealed nanocomposite. The increased crystallization temperature from 115 °C of neat PP to 121 °C of the nanocomposite indicates that the nanoparticles had a strong nucleation effect. Due to the presence of many heterogeneous nucleating agents, the sizes of the spherulites should be reduced significantly as reported previously.[5] An extensive review of SEM micrographs of unannealed and annealed samples did not reveal the presence of any spherulites. TEM micrographs of unannealed and annealed samples, as shown in Figures 6a and b, respectively, do not show the presence of spherulites either.

The morphological changes caused by annealing were analyzed by XRD and DSC. Figure 7 shows XRD spectra of

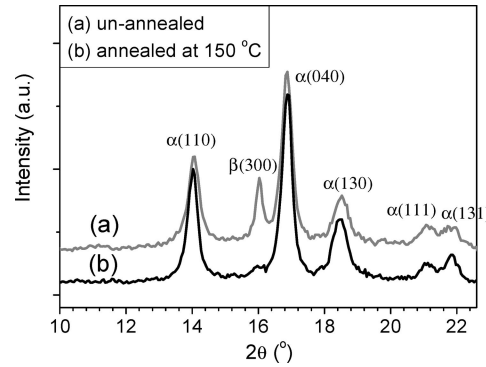

Figure 7. XRD spectra of annealed and unannealed nanocomposites.

unannealed and annealed samples. The curve of the unannealed sample was shifted up by 300 arbitrary units. The characteristic peak (300) of the β phase almost disappeared after annealing at 150 °C for 2 h. In fact, this result is consistent with the PP time−temperature-crystallization diagram[15] and similar results have been obtained by other researchers.[15,23,36,37] At 150 °C, the β phase transforms to the α phase. These XRD results clearly indicate that the β phase, though having high impact toughness, is not the cause for the high impact strength of the annealed nanocomposite.

Figure 8 shows the DSC melting curves of the unannealed and annealed samples. In the unannealed sample, the small peak at 146 °C is indicative of the presence of a small amount of the β phase, which was also detected in the XRD spectrum. The melting of the annealed nanocomposites started at a higher temperature, indicating an increase in the lamellar thickness upon annealing. A noticeable change upon annealing in the DSC curve is the significant growth of an endothermic shoulder at about 152 °C, implying that a microstructural evolution was generated by the heat treatment. It should be pointed out that the endothermic shoulder does not represent multiple phases because only the α phase was detected in the XRD spectrum. The endothermic peak may represent a group of α phase lamellae but with less thermal stability.

The causes of the two endotherms in the fusion of α PP have been studied.[28,29] Petraccone et al.[38] proposed that the two endotherms were due to a partial melting and recrystallization

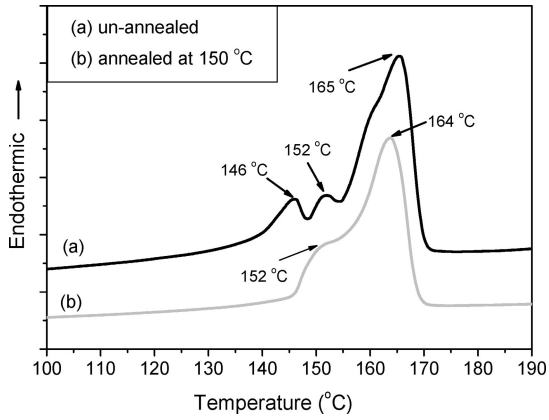

Figure 8. DSC heating scans of annealed and unannealed nanocomposites.

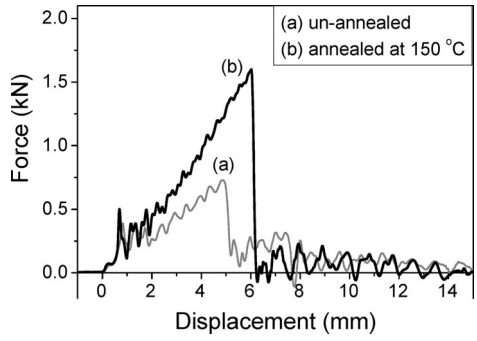

Figure 9. Load-displacement curves of annealed and unannealed nanocomposites obtained in the instrumented falling-weight impact test.

process. A high-temperature melting peak is associated with the melting of the recrystallized lamellae formed during the heating scanning, which were originally thinner and less perfect because they were formed at a lower crystallization temperature. According to this argument, the area of the high-temperature melting peak should decrease with the heating rate. However, the ratio of the peak area at the high temperature to that at the low temperature of the annealed sample did not change when the heating rate decreased from 10 to 5 °C/min. Hence, the endothermic peak is not due to the artifact of heating.

The endothermic shoulder is likely due to the unique cross-hatched structure of PP in which radial and tangential lamellae coexist.[39,40] As shown by Janimak et al.,[41] the radial lamellae have a larger lamellar thickness than the tangential lamellae have if PP crystallizes at a small degree of supercooling. In contrast, if PP crystallizes at a low temperature, the radial and tangential lamellae have similar lamellar thicknesses. The melting of the radial and tangential lamellae with different lamellar thicknesses at different temperatures causes two endothermic peaks when PP crystallizes at high temperatures. This is confirmed by the consistency of the birefringence change of the spherulites when the temperature was increased to the melting temperature of the tangential lamellae, as shown by Alamo et al.[37] At 150 °C, melting and recrystallization occurred, resulting in the cross-hatched structure with thicker radial lamellae and thinner tangential lamellae. Therefore, the endothermic shoulder, which appeared after annealing, likely represents the melting of the tangential lamellae formed during annealing. The TEM micrographs of the unannealed and annealed samples shown in Figure 6 also reveal the enhancement of the cross-hatched structure after annealing.

3.3. Investigation of the Fracture and Toughening Mechanisms. To determine the toughening mechanism, the major energy-consumption term must first be identified. Instrumented falling-weight impact tests were conducted to measure the energy consumption profile of the samples during the impact process. Representative load-displacement curves of annealed and unannealed nanocomposites are depicted in Figure 9. These two curves show that the impact forces increase up to a maximum value and then quickly drop to zero, implying that most energy is consumed in the initiation stage while little energy is dissipated in the fast-crack-propagation stage. Figure 9 clearly shows that the annealed nanocomposite can sustain a fracture force of about 1600 N, much higher than 700 N of the unannealed sample. This implies that a higher force is needed to initiate a crack in an annealed nanocomposite. In addition, the displacement of the annealed sample is larger than that of the unannealed one. The fracture energy, roughly determined by half of the product of the fracture force and the displacement, of the annealed sample is much larger than that of the unannealed one. This suggests that the high toughness of the annealed nanocomposite is due to the high energy absorption in the crack-initiation stage. SEM micrographs of unannealed and annealed nanocomposites visibly support this argument. Parts a−c of Figure 10 are SEM micrographs taken from the fracture surface of an annealed sample at the notch root at different magnifications. The crack-propagation direction is indicated with an arrow in the graphs. The crack-initiation region next to the notch front is divided into two subregions (A and B) according to different degrees of plastic deformation as labeled with dotted lines in Figure 10a. Close-up views of the subregions are presented in Figure 10, parts b and c. The surface of subregion A, which appears to be relatively smooth, as shown in Figure 10b, might be caused by the adiabatic heating generated during the fracture. A rough surface with sheet-like sheared fragments is observed in subregion B, as shown in Figure 10c. The micromorphology of the fracture surface suggests that intensive plastic deformation occurred during the Izod impact. The extent of the plastic deformation can be viewed through the cross-section of a broken Izod sample in a plane perpendicular to the fracture surface. Figure 11a shows the bulk morphology underneath the impact fracture surface of an annealed sample. The sampling location with respect to the broken impact bar is illustrated by the diagram at left-hand side of Figure 11a. The crack-propagation direction is indicated with a white arrow. The boundary of the plastic deformation zone, which is visible and defined by the whitening belt, is marked by a dotted line. At the location, as indicated with a vertical double-headed arrow in Figure 11a, the depth of the plastic deformation zone is approximately 150 μm. Away from the notch root, the severity of the plastic deformation decreases, as displayed in a series of micrographs, shown in Figure 11b−e. The locations, from where the micrographs were taken, are labeled with ①, ②, ③, and ④ in Figure 11a. In the area near the notch root (100 μm away), labeled with ① (c.f., Figure 11b), nanoparticles are aligned along the crack propagation direction. This may be the result of the co-operative movements of the nanoparticles with the shearing of the ligaments. In the area 150 μm away from the notch root, labeled with ② (cf., Figure 11c), the ligaments are highly fibrillated. In an area further away from the notch root (250 μm away), labeled as ③ (cf., Figure 11d), dilated voids are observed, resulting from the moderate stretching of the surrounding ligaments. Debonding of the nanoparticles from the matrix is observed on the whole plastic deformation region (cf., Figure 11b−e). In particular, debonding is still visible in the region about 400 μm away from the notch root, as labeled with ④ (cf., Figure 11e). The examination of the fracture surface and the bulk morphology of a broken

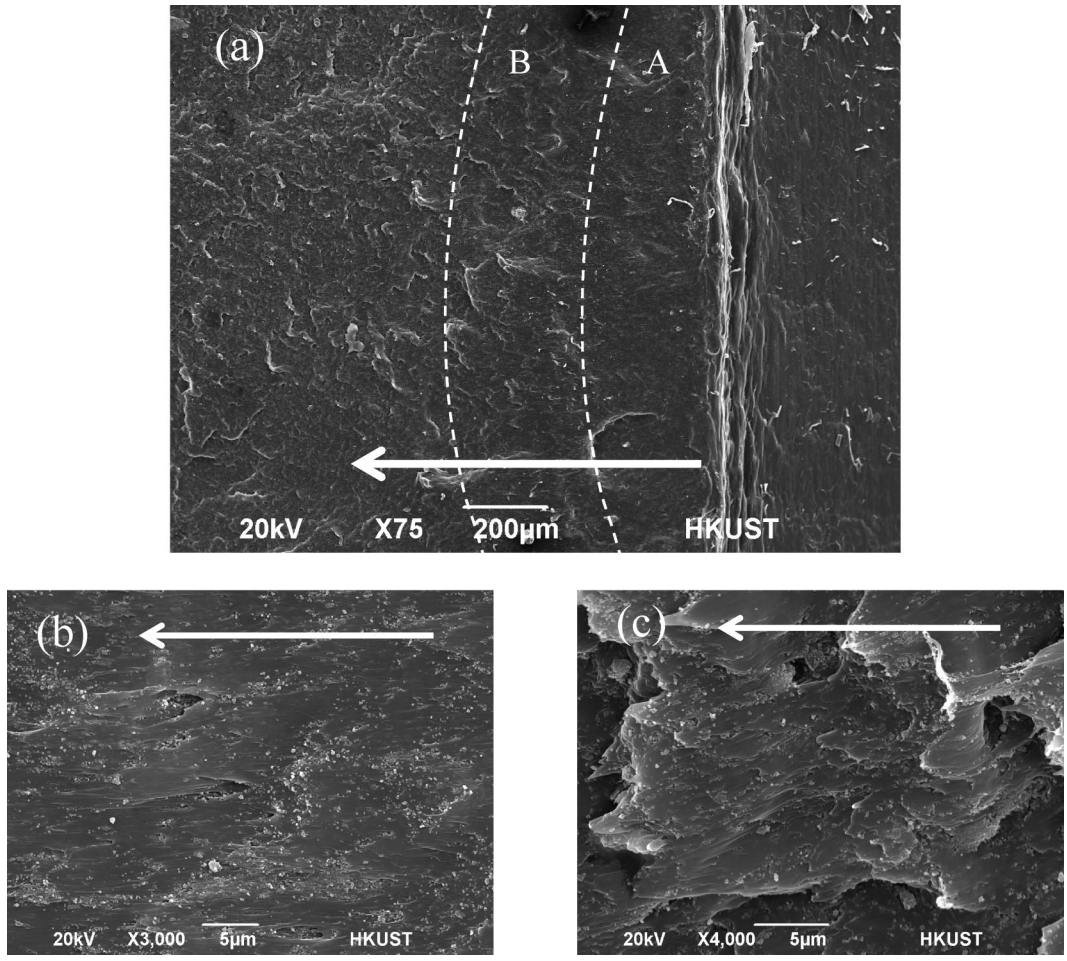

Figure 10. (a) SEM micrograph of an impact fracture surface at the notch root of an annealed nanocomposite; (b) an enlarged view of subregion A in Figure 10a; (c) an enlarged view of subregion B in Figure 10a.

annealed sample from the Izod test confirmed that intensive and extensive plastic deformation takes place at the initiation stage of the impact, which is the reason for the high impact strength of the annealed nanocomposite. For comparisons, the fracture surface and bulk morphology of a broken unannealed sample from the Izod test are shown in Figures 12 and 13, respectively. No sign of plastic deformation can be observed. Debonding is not distinct in the unannealed nanocomposite. These observations are consistent with lower impact strength.

The methodology of capturing the crack-initiation process through an arrested crack tip has been established.[42] To understand the fracture and toughening mechanisms, it is important to investigate how a crack is initiated and accompanied by large energy consumption. The micromorphology of an arrested crack tip of an annealed nanocomposite was examined by SEM. Figure 14 shows two micrographs of an arrested crack tip in an annealed nanocomposite sample at different magnifications. The sampling location with respect to the impact bar is illustrated in the diagram inserted in the right bottom corner of Figure 14a. The crack-propagation direction is indicated with a white arrow. A large plastic deformation zone ahead of the arrested crack tip can be seen in Figure 14a. The crack propagated through the breakage of highly stretched and fibrillar ligaments, as evidenced in Figure 14b. A more clear and striking view can be observed on the TEM micrograph of a thin section containing the arrested crack tip, as shown in Figure 15. The large microvoids are formed as a result of the coalescence of neighboring voids. It seems that as long as the majority of ligaments at the crack tip are not broken, the crack is still stable and fast crack propagation does not start yet. Stronger ligaments can sustain a higher fracture force. This suggests that the great difference in the fracture forces observed in the instrumented falling-weight impact tests between the annealed and unannealed samples is due to their different ligament strengths. In addition, the deformed ligaments blunt the crack tip to some extent, leading to the release of the stress concentration at the crack tip. This blunting effect can also increase the fracture force considerably.

From the micrographs of the arrested crack tip observed by SEM and TEM, we can deduce the fracture mechanism. First, due to the stress concentration, the nanoparticles debond from the PP matrix. Second, as a result of the debonding, the plastic constraints are released and the ligaments undergo plastic deformation. Third, as the deformation continues, a microcrack is formed through the coalescence of the neighboring microvoids due to the breakage of a large number of the ligaments. Finally, the microcrack develops into a macro-crack and catastrophic failure then occurs. Provided that the shear yielding of the ligaments happens in a large volume of the PP matrix, a remarkable amount of energy will be dissipated, leading to the high toughness of the annealed nanocomposite.

3.4. Toughening Mechanism of Annealed Nanocomposite. SEM observations on the impact fracture surface and the bulk morphology underneath the fracture surface confirm that the plastic deformation in the initiation stage is responsible for the high toughness of the annealed nanocomposite. The micromorphology of the arrested crack tip indicates that the crack propagation is via the shear-to-rupture of the ligaments at the crack tip. The results of the instrumented falling-weight impact

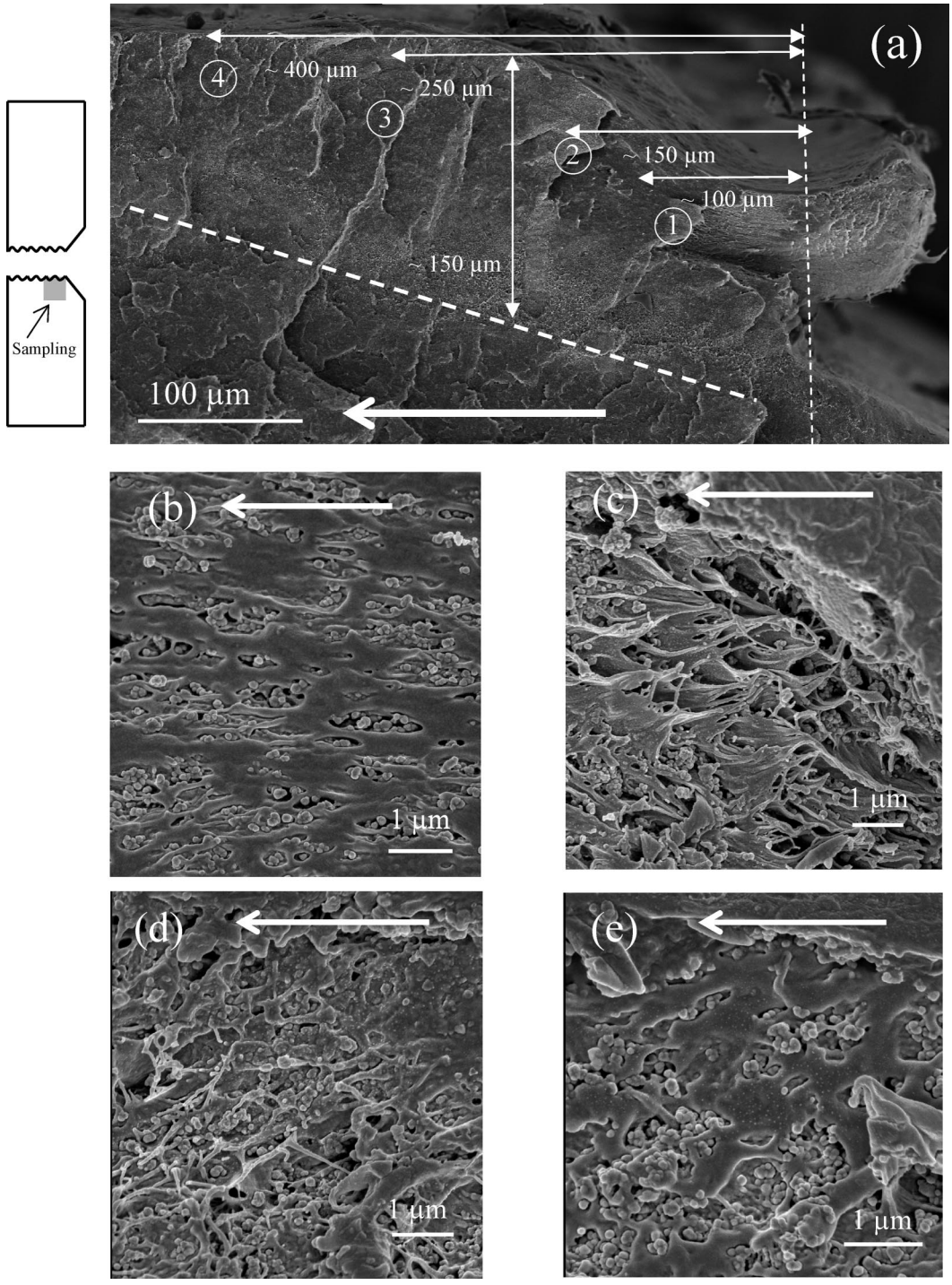

Figure 11. (a) SEM micrographs of the cross-section of a broken Izod annealed nanocomposite; (b−e) magnified micrographs taken in the locations as indicated with ①, ②, ③, and ④, respectively in Figure 11a.

tests revealed that the annealed nanocomposite can sustain a higher facture force than the unannealed one can. Strong ligaments can prevent earlier void coalescence, allowing for a larger plastic deformation zone to develop. As a result, the energy consumed in the initiation stage is substantial. We therefore postulate that the development of a large plastic deformation zone and higher consumption of fracture energy are due to the strong ligaments in the annealed nanocomposite.

The strengthening of the ligaments in the annealed nanocomposite could be the effect of annealing. Figure 16 shows the Izod impact strength of nanocomposites annealed at different temperatures, revealing that the impact strength reaches its maximum at 155 °C. An extensive analysis of the SEM and TEM micrographs indicates that spherulites are absent in both annealed and unannealed samples. Hence, it is safe for us to assume that interspherulitic failure is absent. Annealing at high temperatures changes the microstructures, including thickening of the lamellae and reduction of defects in the lamellae. These changes in the microstructure increase the intrinsic impact toughness of the PP matrix if the concentration of the tie molecules stays relatively constant. However, at high enough temperatures, the melting and recrystallization process reduces the concentration of tie molecules. This will lower the impact toughness of the nanocomposites. In addition, the concentration of the cross-hatched structure altered by annealing may be another factor influencing the impact toughness. According to

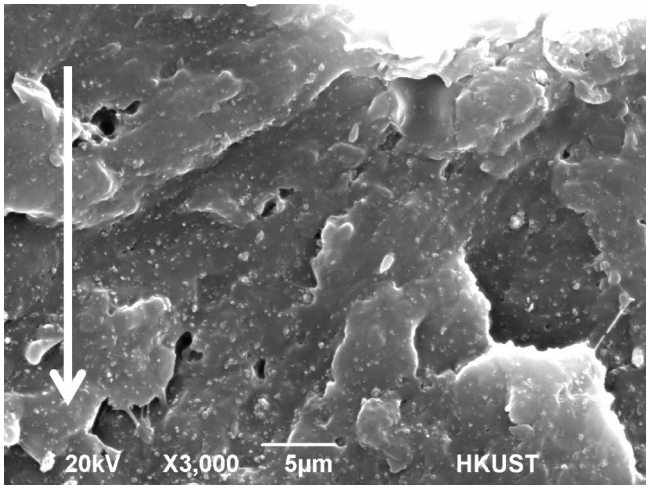

Figure 12. SEM micrograph of an impact fracture surface of an unannealed nanocomposite at the notch root.

a recent atomic force microscopy study on the lamellar growth of iPP, the maximum concentration of the cross-hatched lamellae appeared at about 153 °C.[43] DSC heating scans of our samples, as shown in Figure 17, indicate that the endothermic shoulder, which is attributed to the presence of the cross-hatched structure, shifts to a slightly higher temperature when the annealing temperature changes from 150 to 155 °C and disappears at 160 °C. This suggests that the nanocomposite annealed at 160 °C does not have a cross-hatched structure, which is consistent with the findings in the literature.[43,44] As shown in Figure 16, the impact toughness of the samples annealed at 160 °C is lower than that of the samples annealed at 150 and 155 °C. It is possible that the absence of the cross-hatched structure partially explains the weakening of the ligaments. However, the reduction of impact toughness at 160 °C can be caused mainly by the loss of the tie molecules during high-temperature annealing.

Ishikawa et al. proposed that the strength of the fibrils of the craze is one of the determining factors for the toughness of PP.[45,46] An increase in the fibril strength can sustain a higher stress and allow the expansion of the local plastic zone until the critical stress level is reached, causing the microrupture of the fibrils.[46] The matrix ligaments of the nanocomposites are similar to the fibrils of the craze, both of which control the onset of the catastrophic cracking and the extent of plastic deformation. Hence, we propose that the stronger ligaments are likely responsible for the larger plastic deformation zone of the annealed samples.

Although the strength of the ligaments strengthened by annealing is proposed to be the major reason for the high toughness of the annealed nanocomposite, the effect of annealing on debonding stress, which may influence the impact toughness, cannot be disregarded completely. At this moment, whether the debonding stress increases or decreases after annealing is unknown to us. However, the debonding stress changed by annealing, if any, is insignificant to the annealing-induced high toughness. First, a lower debonding stress might lower the yield stress, which is one of the factors determining the scale of the plastic deformation zone. However, according to the tensile test data, as shown in Table 1, annealing did not give rise to a lower yield stress in the annealed nanocomposite. Therefore, even if the debonding stress became lower after annealing, it is not responsible for the high toughness of the annealed nanocomposite because the large plastic deformation zone does not result from a lower yield stress in the annealed nanocomposite. Second, the debonding stress might have increased after annealing possibly due to an increase in the interaction between nanoparticles and the PP matrix, as shown by the results summarized in Table 1. A careful analysis of the data revealed that the Young modulus and the crystallinity of the nanocomposites increased by 26 and 25%, respectively, after annealing. However, a 10% increase in the Young modulus accompanied by a 16% increase in crystallinity was observed for the neat PP after annealing. A comparison of the Young modulus and crystallinity data between the nanocomposites and the neat PP indicates that the increase in the Young Modulus of the annealed nanocomposite is much higher than that of the annealed neat PP relative to their increases in crystallinity after annealing. The relatively large increase in the Young modulus of the annealed nanocomposite suggests that there might be other factors that affect the Young modulus in addition to the increase in crystallinty. One of the most likely factors is the increased interaction between the $CaCO_3$ nanoparticles and the PP matrix, leading to a higher debonding stress. However, the increase in the interaction should be relatively small because debonding was still observed in the annealed nanocomposite during the tensile test. Nevertheless, the effects of annealing on the debonding stress need a further investigation to provide a more comprehensive understanding of annealing-induced high impact toughness.

It is worth pointing out that one of the preconditions for high impact toughness is the occurrence of nanoparticle debonding, which releases the triaxial tension state of the ligaments, rendering the plastic deformation of the ligaments at the initiation stage feasible. Debonding is seen at the fracture surface in our samples. It is also necessary to mention the benefits

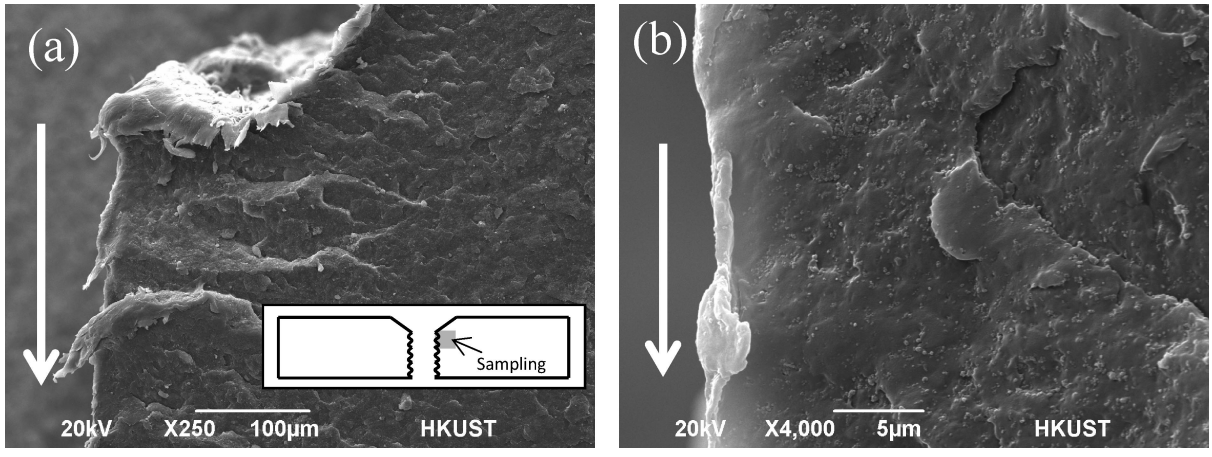

Figure 13. SEM micrographs of a cross-section underneath the impact fracture surface of an unannealed nanocomposite: (a) low magnification; (b) high magnification.

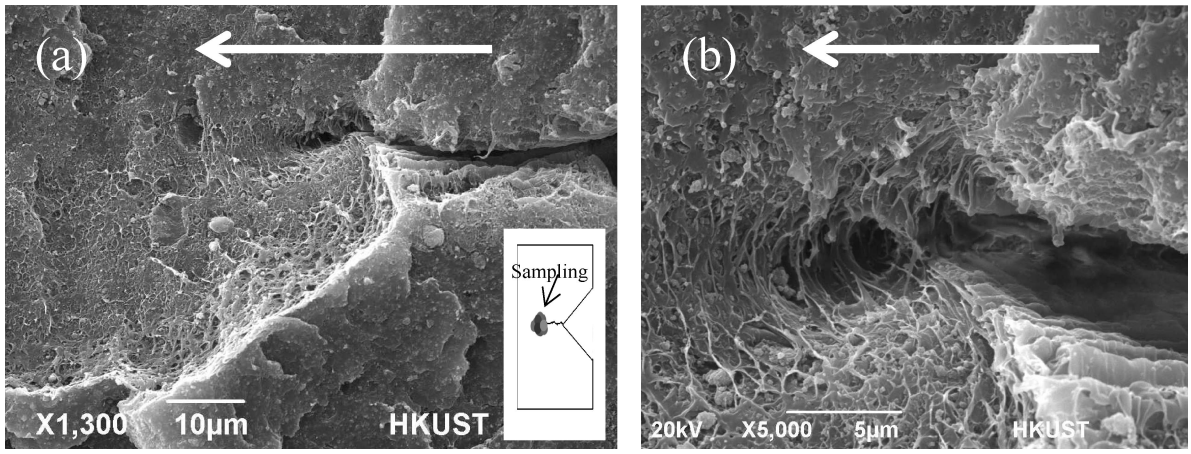

Figure 14. SEM micrographs of an arrested crack tip in an annealed nanocomposite: (a) low magnification; (b) high magnification.

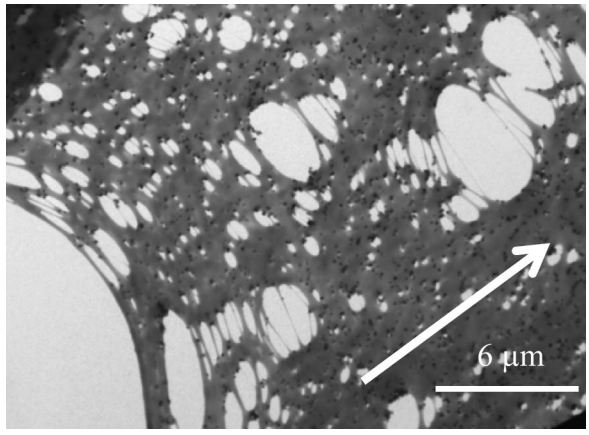

Figure 15. TEM picture of a thin section containing the arrested crack tip of an annealed nanocomposite.

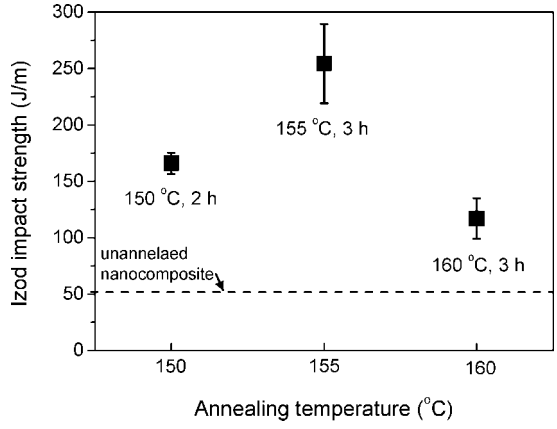

Figure 16. Izod impact strength of nanocomposites with different annealing conditions.

brought by nanoparticles. If the nanoparticles are a nucleating agent, the reduction of the spherulite sizes or the total absence of the spherulites can eliminate interspherulitic failure.[22] Another advantage of the use of nanoparticles instead of microsized particles to toughen PP is that a nanosized filler can create more voids than a microsized filler can with the same filler weight percentage, resulting in more polymeric material being involved in the plastic deformation process. In addition, voids created by a nanofiller are originally smaller and more stable than those created by a microfiller, avoiding early brittle fracture. Of course, the main disadvantage of using nanoparticles is that they are difficult to disperse uniformly in a polymer matrix.

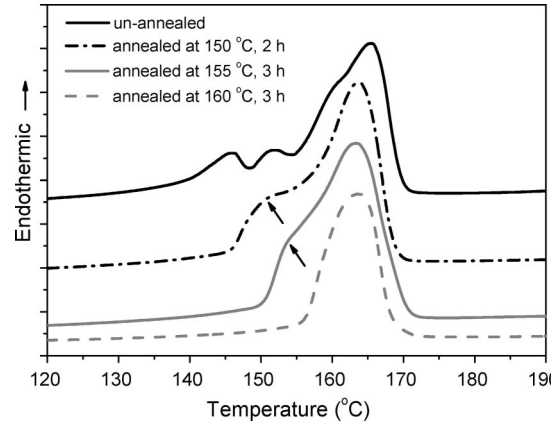

Figure 17. DSC heating scans of nanocomposites with different annealing conditions.

As discussed above, we propose that the high impact toughness of the annealed nanocomposite in this study is the results of three factors working together: (1) good dispersion of nanoparticles; (2) debonding of the nanoparticles at relatively low stress levels; (3) ligaments with high strength. In other words, the high toughness of the annealed nanocomposite is caused by the intensive and extensive plastic deformation happening at the crack initiation stage, which is implemented by the annealing-reinforced ligaments.

4. Conclusion

Good dispersion of nanoparticles is essential and is achieved by coating the nanoparticles with a monolayer of stearic acid. Nanoparticles can dramatically improve the impact strength of i-PP under certain circumstances. The effect of annealing on the impact strength of the PP nanocomposites is tremendous. The high toughness is attributed to the large plastic deformation zone formed in the crack-initiation stage of the impact test. XRD results confirm that the α phase is exclusively present in the annealed nanocomposite, excluding the toughening possibility from the β phase. DSC curves suggest the formation of the cross-hatched structure and the thickening of the radial lamellae after annealing. These morphological changes resulting from annealing are expected to increase ligament strength, which prevents earlier coalescence of microvoids. As a result, a large plastic deformation zone accompanied by large energy consumption can develop. The formation of the large- scale plastic deformation zone was proposed to be caused by two factors. One is the debonding of the nanoparticles from the PP matrix, releasing the triaxial tension state of the ligaments. The other

is the increased strength of the ligaments due to annealing, which promotes large-scale plastic deformation. Of course, further investigations on the effects of annealing and the cross-hatched structure on ligament strength are needed. These works are in progress.

Acknowledgment. This study was financially supported by the Hong Kong Government Research Grants Council under Grants HKUST 610906 and 621306. The assistance given by the Materials Characterization and Preparation Facility and the Advanced Engineering Materials Facility is highly appreciated. Special thanks are extended to Prof. Volker Altstädt of Bayreuth University, Germany, for assistance in the instrumented falling-weight impact tests.

References and Notes

(1) Mcgenity, P. M.; Hooper, J. J.; Paynter, C. D.; Riley, A. M.; Nutbeem, C.; Elton, N. J.; Adams, J. M. *Polymer* **1992**, *33*, 5215–5224.
(2) Jancar, J.; Dibenedetto, A. T.; Dianselmo, A. *Polym. Eng. Sci.* **1993**, *33*, 559–563.
(3) Zuiderduin, W. C. J.; Westzaan, C.; Huetink, J.; Gaymans, R. J. *Polymer* **2002**, *44*, 261–275.
(4) Thio, Y. S.; Argon, A. S.; Cohen, R. E.; Weinberg, M. *Polymer* **2002**, *43*, 3661–3674.
(5) Chan, C. M.; Wu, J. S.; Li, J. X.; Cheung, Y. K. *Polymer* **2002**, *43*, 2981–2992.
(6) Kim, G. M.; Michler, G. H. *Polymer* **1998**, *39*, 5689–5697.
(7) Levita, G.; Marchetti, A.; Lazzeri, A. *Polym. Comp.* **1989**, *10*, 39–43.
(8) Zhang, Q. X.; Yu, Z. Z.; Xie, X. L.; Mai, Y. W. *Polymer* **2004**, *45*, 5985–5994.
(9) Kim, G. M.; Michler, G. H.; Gahleitner, M.; Fiebig, J. *J. Appl. Polym. Sci.* **1996**, *60*, 1391–1403.
(10) Yang, K.; Yang, Q.; Li, G. X.; Zhang, Y.; Zhang, P. *Polym. Eng. Sci.* **2007**, *47*, 95–102.
(11) Price, G. J.; Ansari, D. M. *Polym. Int.* **2004**, *53*, 430–438.
(12) Ahsan, T.; Taylor, D. A. *J. Adhes.* **1998**, *67*, 69–79.
(13) Thio, Y. S.; Argon, A. S.; Cohen, R. E. *Polymer* **2004**, *45*, 3139–3147.
(14) Yang, K.; Yang, Q.; Li, G. X.; Sun, Y. J.; Feng, D. C. *Mater. Lett.* **2006**, *60*, 805–809.
(15) Labor, T.; Gauthier, C.; Seguela, R.; Vigier, G.; Bomal, Y.; Orange, G. *Polymer* **2001**, *42*, 7127–7135.
(16) Labor, T.; Vigier, G.; Seguela, R.; Guathier, C.; Orange, G.; Bomal, Y. *J. Polym. Sci., Part B: Polym. Phys.* **2002**, *40*, 31–42.
(17) Friedrich, K. *Prog. Colloid Polym. Sci.* **1978**, *64*, 103–112.
(18) Wang, G.; Chen, X. Y.; Huang, R.; Zhang, L. *J. Mater. Sci. Lett.* **2002**, *21*, 985–986.
(19) Tabtiang, A.; Venables, R. *Eur. Polym. J.* **2000**, *36*, 137–148.
(20) Lazzeri, A.; Zebarjad, S. M.; Pracella, M.; Cavalier, K.; Rosa, R. *Polymer* **2005**, *46*, 827–844.
(21) Osman, M. A.; Atallah, A.; Suter, U. W. *Polymer* **2004**, *45*, 1177–1183.
(22) Way, J. L.; Atkinson, J. R.; Nutting, J. *J. Mater. Sci.* **1974**, *9*, 293–299.
(23) Ferrer-Balas, D.; Maspoch, M. L.; Martinez, A. B.; Santana, O. O. *Polymer* **2001**, *42*, 1697–1705.
(24) Frontini, P. M.; Fave, A. *J. Mater. Sci.* **1995**, *30*, 2446–2454.
(25) Drozdov, A. D.; Christiansen, J. D. *Eur. Polym. J.* **2003**, *39*, 21–31.
(26) Seguela, R.; Staniek, E.; Escaig, B.; Fillon, B. *J. Appl. Polym. Sci.* **1999**, *71*, 1873–1885.
(27) Poussin, L.; Bertin, Y. A.; Parisot, J.; Brassy, C. *Polymer* **1998**, *39*, 4261–4265.
(28) Hedesiu, C.; Demco, D. E.; Kleppinger, R.; Vanden Poel, G.; Gijsbers, W.; Bluemich, B.; Remerie, K.; Litvinov, V. M. *Macromolecules* **2007**, *40*, 3977–3989.
(29) Martorana, A.; Piccarolo, S.; Sapoundjieva, D. *Macromol. Chem. Phys.* **1999**, *200*, 531–540.
(30) Clark, E. J.; Hoffman, J. D. *Macromolecules* **1984**, *17*, 878–885.
(31) Li, J. X.; Cheung, W. L. *J. Appl. Polym. Sci.* **1999**, *72*, 1529–1538.
(32) Osman, M. A.; Suter, U. W. *Chem. Mater.* **2002**, *14*, 4408–4415.
(33) Morimoto, T.; Kishi, J.; Okada, O.; Kadota, T. *Bull. Chem. Soc. Jpn.* **1980**, *53*, 1918–1921.
(34) Fekete, E.; Pukanszky, B.; Toth, A.; Bertoti, I. *J. Colloid Interface Sci.* **1990**, *135*, 200–208.
(35) Lazzeri, A.; Thio, Y. S.; Cohen, R. E. *J. Appl. Polym. Sci.* **2004**, *91*, 925–935.
(36) Kotek, J.; Keinar, I.; Baldrian, J.; Raab, M. *Eur. Polym. J.* **2004**, *40*, 2731–2738.
(37) Alamo, R. G.; Brown, G. M.; Mandelkern, L.; Lehtinen, A.; Paukkeri, R. *Polymer* **1999**, *40*, 3933–3944.
(38) Petraccone, V.; Guerra, G.; De Rosa, C.; Tuzi, A. *Macromolecules* **1985**, *18*, 813–814.
(39) Maiti, P.; Hikosaka, M.; Yamada, K.; Toda, A.; Gu, F. *Macromolecules* **2000**, *33*, 9069–9075.
(40) Al-Raheil, I. A.; Qudah, A. M.; Al-Share, M. *J. Appl. Polym. Sci.* **1998**, *67*, 1259–1265.
(41) Janimak, J. J.; Cheng, S. Z. D.; Giusti, P. A.; Hsieh, E. T. *Macromolecules* **1991**, *24*, 2253–2260.
(42) Wu, J. S.; Mai, Y. W. *J. Mater. Sci.* **1993**, *28*, 6167–6177.
(43) Zhou, J. J.; Liu, J. G.; Yan, S. K.; Dong, J. Y.; Li, L.; Chan, C. M.; Schultz, J. M. *Polymer* **2005**, *46*, 4077–4087.
(44) Bassett, D. C.; Olley, R. H. *Polymer* **1984**, *25*, 935–943.
(45) Ishikawa, M.; Ushui, K.; Kondo, Y.; Hatada, K.; Gima, S. *Polymer* **1996**, *37*, 5375–5379.
(46) Sugimoto, M.; Ishikawa, M.; Hatada, K. *Polymer* **1995**, *36*, 3675–3682.

MA801095D